PHOTONICS Research

Trans-spectral transfer of spatio-temporal optical Ferris wheel with nonlinear wave mixing

SANDAN WANG,[1,2] JINPENG YUAN,[1,2,*] LIRONG WANG,[1,2,3] LIANTUAN XIAO,[1,2] AND SUOTANG JIA[1,2]

[1]State Key Laboratory of Quantum Optics and Quantum Optics Devices, Institute of Laser Spectroscopy, Shanxi University, Taiyuan 030006, China
[2]Collaborative Innovation Center of Extreme Optics, Shanxi University, Taiyuan 030006, China
[3]e-mail: wlr@sxu.edu.cn
*Corresponding author: yjp@sxu.edu.cn

The trans-spectral manipulation of spatio-temporal structured light, characterized by dynamic inhomogeneous trajectories and a unique nature in the space–time domain, opens myriad possibilities for high-dimensional optical communication in the ultraviolet band. Here, we experimentally demonstrate the high-performance transfer of the spatio-temporal optical Ferris wheel beam from near-infrared to blue–violet wavelengths. Owing to the energy conservation and momentum conservation mechanism, the 420 nm output signal beam accurately retains the spatio-temporal characteristics of the 776 nm input probe optical Ferris wheel beam, facilitated by the 780 nm Gaussian pump beam. The identical multi-petal intensity profiles confirm the successful transfer of spatial characteristics from the input probe to the output signal beams. The fully synchronized rotation velocities and directions of the probe and signal beams demonstrate the precise transfer of temporal characteristics, achieving approximately 98% conversion accuracy. This work enables efficient information transfer across different wavelength bands and offers a promising approach for achieving high-dimensional quantum communication.   ©2024 Chinese Laser Press

1. INTRODUCTION

Extending physical dimensions of the photons with frequency, amplitude, phase, and polarization enables a diversity of light-related applications [1–6]. The introduction of orbital angular momentum (OAM) with infinite orthogonal modes in the spatial domain extends beyond the transverse plane, enabling the tailoring of light in three-dimensional fields [7]. Taking a step further, combining OAM with time enables the sculpting of spatio-temporal structured light beyond the spatial domain into a four-dimensional field, paving the way for pioneering research in high-dimensional quantum communication [8,9].

Spatio-temporal optical Ferris wheel (OFW) beams, characterized by distinct spatial and temporal imprinting, are generated through the coordinated modulation of the spatial distribution and temporal variation of two different OAM modes. Conventional methods for generating and manipulating spatio-temporal OFW beams typically rely on the linear optical elements, such as axially symmetric polarization elements, nested spiral-array plates, vortex phase plates, and spatial light modulators [10–14]. However, the above optical elements in the blue–violet wavelength range face several challenges, including complex manufacturing processes, specialized material

requirements, low damage thresholds, and high costs. Trans-spectral manipulation of spatio-temporal OFW beams, shifting from one input frequency to an entirely different frequency, offers a promising solution. This approach can potentially establish a wavelength bridge, which is crucial for advancing high-dimensional quantum information processing [15].

Nonlinear frequency conversion facilitates the transfer of physical dimensions between different wavebands, eliminating frequency gaps through processes such as harmonic generation, sum-frequency generation, difference-frequency generation, and multi-wave mixing [16–21]. Compared with the nonlinear crystals, the atomic vapor offers unique advantages of flexible controllability, easily saturated characteristic, and high power handling capability, making it an increasingly promising candidate as a nonlinear medium [22–26]. The phase-matching capability enabled by energy and momentum conservation ensures the successful transfer of phase information associated with OAM modes in atomic vapor through nonlinear frequency conversion [27–30]. These studies provide robust support for the transfer of the spatio-temporal OFW beams across different wavelengths by nonlinear frequency conversion in atomic vapor. To the best of our knowledge, the experimental manipulation of spatio-temporal OFW beams via nonlinear

frequency conversion in an atomic medium has not yet been explored.

In this work, we experimentally and theoretically demonstrate the high-performance transfer of spatio-temporal OFW beams based on nonlinear frequency conversion. The spatial and temporal characteristics of spatio-temporal OFW beams are efficiently imprinted from near-infrared (776 nm) to blue–violet (420 nm) wavelength in a diamond-type energy level system of ^{85}Rb atoms. The perfectly coincident multi-petal intensity profiles, with varying topological charge differences (Δl) between the input and output spatio-temporal OFW beams, confirm the flawless transfer of spatial characteristics. The isochronous rotation velocities and directions of the beams verify the precise transfer of temporal characteristics, which are accurately controlled by the frequency difference (Δf) of the spatio-temporal OFW beams. Our scheme offers a new possibility for building communication interfaces with different wavebands in quantum science fields based on atomic ensembles.

2. EXPERIMENTAL SCHEME

The trans-spectral transfer principle of the spatio-temporal OFW beam by nonlinear wave mixing is shown in Fig. 1(a). The 780 nm Gaussian pump and 776 nm spatio-temporal OFW probe beams are focused by the lens and interact with ^{85}Rb atoms in a co-propagating configuration to excite the atoms from $5S_{1/2}$ ground state to $5D_{5/2}$ excited state by two-photon absorption. Then, a substantial population inversion on the $5D_{5/2} – 6P_{3/2}$ transition is established, leading to the directional mid-infrared light field at 5233 nm via amplified spontaneous emission. Finally, the 420 nm signal blue–violet OFW beam with spatio-temporal characteristic is effectively generated at the exit end of the Rb vapor in the four-wave mixing (FWM) process. Thus, the transfer of the spatio-temporal OFW beam is completely achieved from input probe to output signal beams. The relevant diamond-type energy level system of ^{85}Rb atoms is shown in the inset of Fig. 1(a).

The relevant experimental setup is divided into two parts: the pulse-to-pulse interferometer and the spatio-temporal OFW beam transfer, which are demonstrated in Figs. 1(b) and 1(c), respectively. The laser source is provided by an optical frequency comb (OFC) system with the comb mode of $f_n = nf_{rep} + f_{ceo}$, where the repetition frequency f_{rep} is 250 MHz, and the offset frequency f_{ceo} is 20 MHz. The Gaussian profile of OFC system is split into two beams by a half-wave plate (HWP) and a polarization beam splitter (PBS1). The transmitted beam with horizontal linear polarization is employed as the reference with $f_{ceo1} = f_{ceo}$. The reflected beam passes through an acousto-optic modulator (AOM) (AA, MT250-A0.5-800) with shifted frequency f_{AOM}, which is driven by a signal source (Rohde & Schwarz, SMB100A) with the frequency accuracy of 10^{-2} and the switching rate of 10 ns. The zeroth-order beam from AOM is obscured by a beam block (BB), and the first-order beam is employed with $f_{ceo2} = f_{ceo} + \Delta f$ as vertically linear polarization. The adjustable $\Delta f = f_{AOM} - f_{rep}$ with a wide range from 10^{-2} to 10^6 Hz is the offset frequency difference of reflected and transmitted beams, providing precise temporal controllability. The time delayer, composed of a hollow roof mirror (HRM) and a linear electric translation stage (Thorlabs, LTS300), allows us to finely tune the optical path difference and thus leads to a pulse-to-pulse interference between the reflected and transmitted beams. Finally, the effective dual-comb beam with Δf is produced by single-mode fiber, which is exhibited in Fig. 1(b).
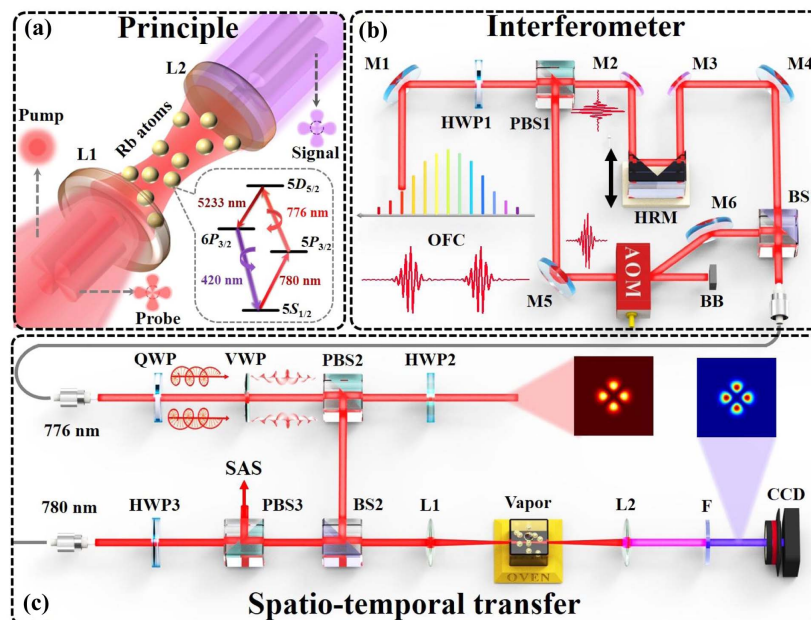
Fig. 1. (a) Principle of the spatio-temporal OFW beam transfer by nonlinear wave mixing. Experimental setup of (b) pulse-to-pulse interferometer and (c) spatio-temporal OFW beam transfer. OFC, optical frequency comb; M, high-reflection mirror; HWP, half-wave plate; PBS, polarization beam splitter; AOM, acousto-optic modulator; BB, beam block; HRM, hollow roof mirror; BS, beam splitter; QWP, quarter-wave plate; VWP, vortex wave plate; L, lens; F, filter; CCD, charge coupled device.

Figure 1(c) depicts the spatio-temporal OFW beam transfer process. The effective dual-comb beam with two overlapped Gaussian profiles is switched to opposite left and right circular polarizations ($\sigma_1 = -1$ and $\sigma_2 = +1$) using a quarter-wave plate (QWP), respectively. The beams with left and right circular polarization ($l_1 = 0$, $\sigma_1 = -1$, $l_2 = 0$, $\sigma_2 = +1$) are converted into the vortex beams with right and left circular polarization ($l_1 = -l$, $\sigma_1 = +1$, $l_2 = +l$, $\sigma_2 = -1$) by a vortex wave plate (VWP) with topological charge l. The spatio-temporal OFW beam with periodic rotating point-symmetry multi-petaled bright spot is generated through the interference between two vortex beams with the identical intensity and the opposite l ($l_1 = -l_2$) at PBS2. The spatial characteristics of the spatio-temporal OFW beam, with a switching rate of 100 ms, are determined by the number of bright spots, which corresponds to the topological charge difference $\Delta l = |l_1 - l_2|$ of two vortex comb beams. The temporal characteristics are determined by the rotation period of $T = \Delta l / \Delta f$. The rotating angular velocities of the generated spatio-temporal OFW beams can be achieved in a wide range from 10^{-3} to 10^6 rad/s by adjusting the Δl and Δf in our experiment.

Furthermore, the generated probe spatio-temporal OFW beam with 776 nm and another 780 nm Gaussian pump beam (TA pro, Toptica) enter a 10 mm × 10 mm × 10 mm thermal vapor cell through the co-propagating configuration to induce the FWM process. The vapor is heated to 130°C with the corresponding atomic density of approximately 3.47×10^{14} m^{-3} for realizing the optimal frequency conversion efficiency. The waist of the pump beam inside the vapor cell is approximately 250 μm, while the waist of the probe beam varies from 88 to 117 μm for different Δl. The minimum Rayleigh length exceeds the thickness of the vapor cell, allowing the Gouy phase matching to be neglected in this FWM process [31]. At the exit end of the vapor cell, the transmitted pump and probe beams are blocked with a filter (center wavelength 420 nm, 10 nm pass band). Finally, a charge coupled device (CCD) is employed to record the generated 420 nm signal spatio-temporal OFW beam in the FWM process.

3. THEORY

The optical vortex with helical phase factor $\exp(il\theta)$ carries OAM of $l\hbar$ per photon, where l is the topological charge, and $\hbar$ is the reduced Planck constant [32]. The electric field of optical vortex with zero radial mode number is expressed as [33]

$$E_v(r, \theta, z) = A_l \exp\left\{i\left[k\left(z - \frac{r^2}{2R}\right) - \omega t + \varphi_l\right]\right\} \exp(-i\varphi_v),$$
(1)

where r, θ, and z are the polar coordinates parameters, $A_l = \sqrt{I}\sqrt{2/\pi l!}(\sqrt{2}r/\omega)^l \exp(-r^2/\omega^2)$ is the dimensionless radial amplitude variation multiplied by the square root of a beam intensity parameter I, $\omega = \omega_0\sqrt{1 + (z/z_R)^2}$ is the beam waist, $z_R = \pi\omega_0^2/\lambda$ is the Rayleigh range, $R = z[1 + (z/z_R)^2]$ is the radius of curvature, ω is the angular frequency, $\varphi_l = (l + 1)\arctan(z/z_R)$ is the Gouy phase, and $\varphi_v = l\theta$ is the spatial phase of optical vortex.

The OFC system is presented as a pulse train with period $T = 1/f_{\text{rep}}$ in the time domain, where f_{rep} is the repetition frequency of the OFC. Due to the medium dispersion effect, the carrier and envelope of the single pulse have phase deviation with the time t accumulation, which is expressed as carrier envelope temporal phase $\varphi_c(t) = 2\pi f_{\text{ceo}}t$, where f_{ceo} is the offset frequency. When superimposing the optical vortex on the OFC, the electric field intensity of vortex comb is expressed as

$$E_{\text{vc}}(r, \theta, z) = A_l \exp\left\{i\left[k\left(z - \frac{r^2}{2R}\right) - \omega t + \varphi_l\right]\right\} \exp(-i\varphi_{\text{vc}}),$$
(2)

where $\varphi_{\text{vc}} = 2\pi f_{\text{ceo}}t + l\theta$ is the spatio-temporal phase. The high controllability of f_{ceo} and l ensures the precise and arbitrary manipulation of the spatio-temporal phase.

The interference occurs between two vortex comb beams with a certain offset frequency difference Δf and opposite topological charges $l_1 = |l_2|$. As a result, a spatio-temporal OFW beam with multi-dimensional controllability is generated, and the beam intensity is determined as

$$I = 2A_l^2[1 + \cos(2\pi\Delta f t + \Delta l\theta)],$$
(3)

where $\Delta l = |l_1 - l_2|$ is topological charge difference. The spatial characteristic of the beam is determined by the angular distribution intensity pattern because of the spatial phase difference ($\Delta\varphi_v = \Delta l\theta$). The temporal characteristic of the beam is characterized by the continuous rotation because of the temporal phase difference ($\Delta\varphi_c = 2\pi\Delta f t$).

The spatio-temporal OFW beam transfer essentially involves the frequency conversion of OAM components of two vortex comb beams:

$$\chi^{(3)}E_{780}E_{776}E^*_{5233} \rightarrow E_{420},$$
(4)

where $\chi^{(3)}$ is the nonlinear susceptibility and E represents the involved light fields. Under the restrictions of the OAM conservation and phase-matching condition, the four light fields satisfy $l_{780} + l_{776} = l_{5233} + l_{420}$ and $f_{780} + f_{776} = f_{5233} + f_{420}$.

When a 780 nm pump Gaussian beam ($\Delta l_{780} = 0$, $\Delta f_{780} = 0$) and a 776 nm probe spatio-temporal OFW beam are used to excite the ^{85}Rb $5S_{1/2} - 5P_{3/2} - 5D_{5/2}$ two-photon transition, the 420 nm output signal blue–violet field E_{420} is generated in the FWM process under collinear beam geometry. The generation of E_{420} satisfies the conservation of angular momentum with $\Delta l_{780} + \Delta l_{776} = \Delta l_{5233} + \Delta l_{420}$ and the conservation of energy with $\Delta f_{780} + \Delta f_{776} = \Delta f_{5233} + \Delta f_{420}$. The $\Delta l_{5233} = 0$ and $\Delta f_{5233} = 0$ are expected because the 5233 nm mid-infrared field is mainly generated by amplified spontaneous emission [34]. The obtained $\Delta l_{420} = \Delta l_{776}$ and $\Delta f_{420} = \Delta f_{776}$ ensure the high-performance consistency of the spatio-temporal OFW beam transfer from near-infrared to blue–violet wavelength. Additionally, the generated 420 nm spatio-temporal OFW beams offer advantages such as spatial resolution on the order of hundreds of nanometers, temporal accuracy on the order of milliseconds, and a tunable power dynamic range from microwatts to milliwatts.

Figure 2(a) depicts the theoretical simulated spatial intensity and phase of the generated 420 nm blue–violet beam when the
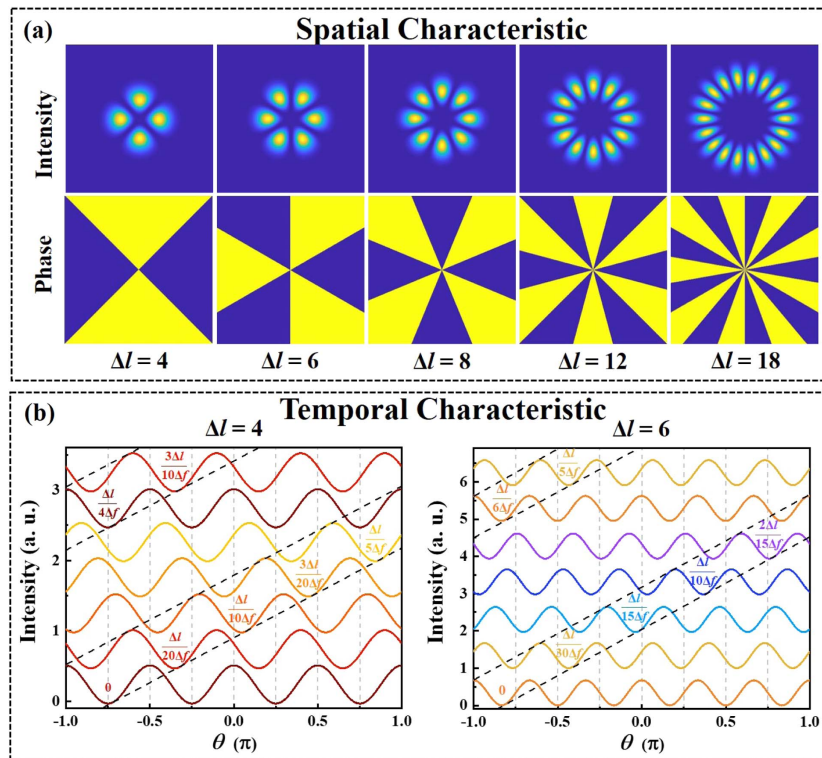
Fig. 2. Theoretical simulation results of generated blue–violet beam by the FWM process. (a) Spatial intensity and phase distribution of blue–violet beam with $\Delta l = 4$, 6, 8, 12, and 18, respectively. (b) Temporal evolution of blue–violet beam azimuthal profile with $\Delta l = 4$ and $\Delta l = 6$, respectively.
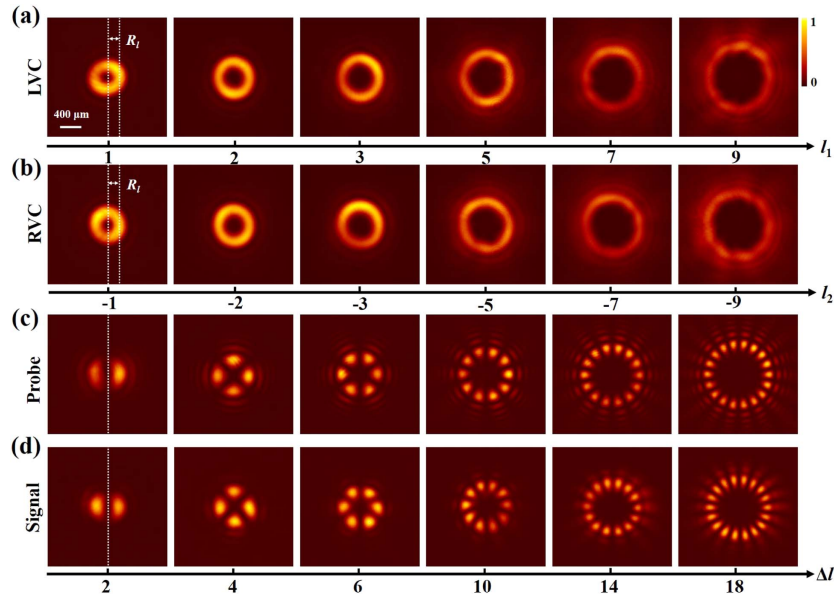
topological charge difference Δl of the 776 nm spatio-temporal OFW beam is 4, 6, 8, 12, and 18, respectively. The intensity pattern of the 420 nm blue–violet beam carries no net angular momentum and forms a ring-shaped structure, consisting of Δl point-symmetric petal-like bright spot along the azimuthal coordinate. The number of bright spots is consistent with the 776 nm spatio-temporal OFW beam when the Δl is the same, indicating that spatial characteristic transfer is achieved successfully from 776 nm near-infrared to 420 nm blue–violet wavelengths.

Additionally, the temporal characteristic transfer of the spatio-temporal OFW beam is characterized by continuously rotating modulation with the $v = 2\pi\Delta f/\Delta l$ rotational angular velocity. Figure 2(b) represents the azimuthal profiles of the generated 420 nm blue–violet beam with different rotation time. The rotation time of a beam bright spot from the initial position to the next position is $\Delta l/4\Delta f$ and $\Delta l/6\Delta f$ when the Δl is 4 and 6, respectively, indicating that the beam rotation period is $T = \Delta l/\Delta f$. The rotation period of the 420 nm beam is consistent well with that of the 776 nm beam. Therefore, the temporal characteristic transfer of the spatio-temporal OFW beam is effectively implemented from 776 nm near-infrared to 420 nm blue–violet beams in the FWM process.

4. RESULTS AND DISCUSSION

The intensity profiles of left circularly polarized vortex comb (LVC) beams with $l_1 = 1$, 2, 3, 5, 7, and 9 are shown in

Fig. 3(a). These beams all exhibit the spatial ring profiles, and the radius R_l linearly increases with the increase of l [35]. The right circularly polarized vortex comb (RVC) beams with $l_2 = -1$, -2, -3, -5, -7, and -9 are described in Fig. 3(b). There is the same profile of vortex comb beams when $l_1 = |l_2|$. Furthermore, the 776 nm spatio-temporal OFW beams are obtained experimentally by the interference of the above two vortex comb beams with the same laser intensity and opposite topological charge $l_1 = |l_2|$, which are shown in Fig. 3(c). The intensity profile of the generated 776 nm spatio-temporal OFW beams shows plentiful spatial distribution with better point-symmetry multi-petaled bright spot. The bright spot numbers $m = 2$, 4, 6, 10, 14, and 18 are determined by the l of two vortex comb beams, which is denoted as $m = \Delta l = |l_1 - l_2|$. The 780 nm pump Gaussian beam and the 776 nm probe spatio-temporal OFW beam are used to excite the ^{85}Rb $5S_{1/2} - 5P_{3/2} - 5D_{5/2}$ two-photon transition experimentally. The generated 420 nm signal beams in FWM process exhibit the same point-symmetry multi-petaled bright spot and matching radius with 776 nm probe beams at the same Δl, indicating that the spatial characteristic of the spatio-temporal OFW beam is effectively transferred from input probe to output signal beams. The frequency conversion efficiency of the 420 nm output signal beam is proportional to the overlap integral of the 780 nm pump beam and the 776 nm probe beam. Additionally, the spatial structure of the output signal beam exhibits slight distortions compared to the input probe beam. This is attributed to variations in phase matching

Fig. 3. Experimental intensity profiles of the vortex comb beams with different topological charges (a) $l_1 = 1, 2, 3, 5, 7,$ and 9 and (b) $l_2 = -1,$ $-2, -3, -5, -7,$ and -9, respectively. Spatial distribution of (c) input 776 nm probe spatio-temporal OFW beams and (d) output 420 nm signal beams with topological charge difference $\Delta l = 2, 4, 6, 10, 14,$ and 18, respectively.

conditions, nonlinear effects during the FWM process, and experimental factors.

The temporal characteristic transfer of the spatio-temporal OFW beam in the FWM process is displayed by the periodic rotation of probe and signal beams at different Δl and Δf. Figure 4(a) depicts the temporal rotation evolutions of 776 nm probe beam and 420 nm signal beam with rotation period of 3 s when the $\Delta l = 6$ and $\Delta f = 2$ Hz. The white arrows indicate the rotation position of a fixed beam bright spot at different times. It can be found that the probe and signal

beams all preserve its six-petaled spatial pattern with clockwise rotation synchronously. In addition, the azimuthal angle ϕ_{max} for the beams' maximum intensity is measured to extract the rotation velocity with the time evolution. The ϕ_{max} of the probe (red dots) and signal (blue dots) beams as a function of the rotation time t is shown in Fig. 4(b) when $\Delta l = 6$ and $\Delta f = 2$ Hz. The dots represent experimental data, and the lines are theoretical fitting results by the function of $\phi_{max} = \phi_0 + vt$, where ϕ_0 is the initial azimuthal angle, and v is the rotation velocity. The ϕ_{max} of probe and signal
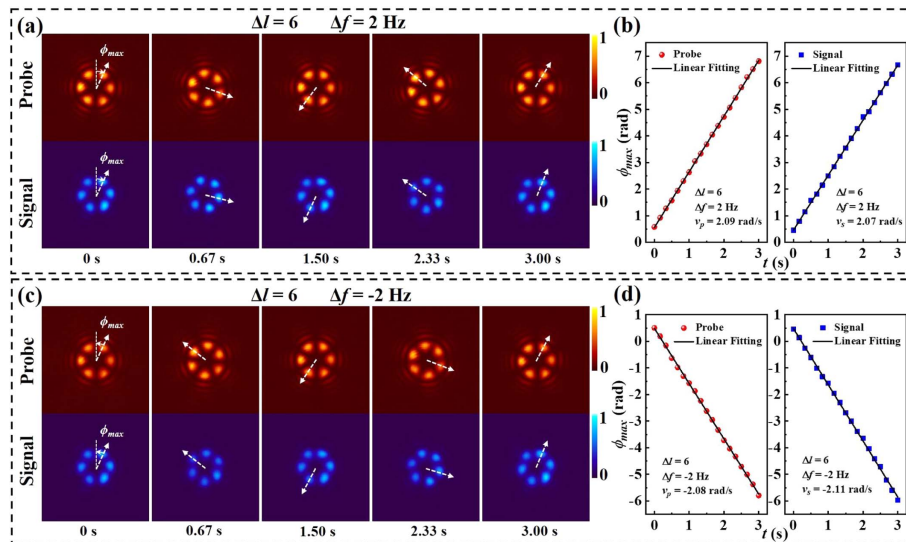
Fig. 4. Temporal characteristic transfer of spatio-temporal OFW beam with $\Delta l = 6$ when $\Delta f = 2$ Hz and $\Delta f = -2$ Hz, respectively. (a) and (c) show the rotating patterns imaged of 776 nm probe and 420 nm signal beams. (b) and (d) show the azimuthal angle for the beam maximum intensity ϕ_{max} as a function of the rotation time.
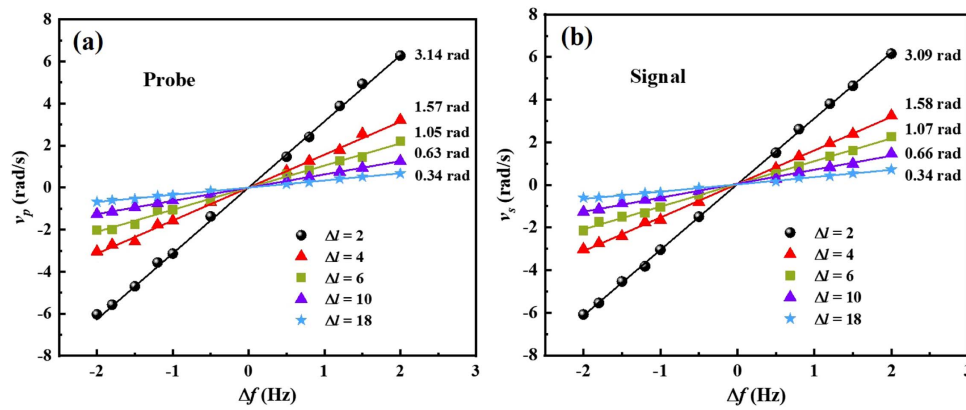
Fig. 5. Rotation velocities of (a) input probe v_p and (b) output signal v_s beams as a function of Δf with $\Delta l = 2, 4, 6, 10,$ and 18, respectively. The dots represent the experimental results, and the lines refer to the theoretical fitting results.

beams increases linearly with the increasing t, corresponding to the $v_p = 2.09$ rad/s of the probe beam and $v_s = 2.07$ rad/s of the signal beam, respectively.

Furthermore, the temporal characteristic transfer of the spatio-temporal OFW beam is described by the rotation direction of probe and signal beams. When the Δf is positive, the probe and signal beams are rotated synchronously in the clockwise direction, which is shown in Fig. 4(a). On the contrary, the rotating direction of the two beams is counterclockwise with the negative value of Δf [Fig. 4(b)]. Meanwhile, the rotation velocity of input probe and output signal beams is $v_p = -2.08$ rad/s and $v_s = -2.11$ rad/s with $\Delta l = 6$ and $\Delta f = -2$ Hz, respectively, as shown in Fig. 4(d). The rotating videos of these two kinds of beams are shown in Visualization 1 and Visualization 2, respectively. These results indicate that the temporal characteristics of the spatio-temporal OFW beam are effectively transferred from the input probe to the output signal beams. Meanwhile, the switching rate of the input probe beam to the output signal beam, on the order of hundreds of nanometers, is primarily determined by the lifetime of Rb atomic energy levels and phase matching conditions. This rate is theoretically limited by natural linewidth of the energy levels and the interaction time between the laser and the atoms.

The temporal characteristics transfer of the spatio-temporal OFW beam in the FWM process is quantitatively characterized by measuring the rotation velocity of probe and signal beams with different Δf and Δl. Figure 5(a) shows the rotation velocity v_p of the 776 nm probe spatio-temporal OFW beam as a function of the Δf for $\Delta l = 2, 4, 6, 10,$ and 18, respectively. The beam rotates in a counterclockwise direction ($v_p < 0$) with the negative Δf while the beam has a clockwise rotation direction ($v_p > 0$) when the Δf is positive. The absolute value of v_p increases with increasing Δf under the constant Δl. The absolute value of v_p decreases with the increase of Δl when the Δf remains constant. The experimental results and linear fitting results are in good agreement. Additionally, the 420 nm signal beam variation trend of v_s versus Δf and Δl is consistent well with that for the case of a 776 nm probe beam, as shown in Fig. 5(b). Meanwhile, the temporal characteristic conversion accuracy of the spatio-temporal OFW beams is kept ~98%

for different Δl, which is defined as $D = 1 - \frac{|\phi_s - \phi_p|}{\phi_p}$, where $\phi_{s(p)} = \frac{v_{s(p)}}{\Delta f}$ is the azimuthal angle of signal and probe beams, $v_{s(p)}$ is the rotation velocity of signal and probe beams, and Δf is the offset frequency difference. The conversion accuracy is compromised when the rotation velocity of the 776 nm probe beam exceeds the response capacity of the Rb atoms. To sum up, the spatio-temporal OFW beam transfer from near-infrared (776 nm) wavelength to blue–violet (420 nm) wavelength in the FWM process is effectively characterized by the beam spatial profile, rotation velocity, and rotation direction of input probe and output signal beams.

5. CONCLUSION

In summary, we realize the high-performance trans-spectral transfer of the spatio-temporal OFW beam with bright petal-like patterns based on nonlinear wave mixing in a ^{85}Rb atomic medium. The spatial and temporal characteristics of spatio-temporal OFW beams are successfully converted from near-infrared wavelength (776 nm) to another completely different wavelength (420 nm). The high-efficiency transfer of spatial characteristics is demonstrated by the identical multi-petal intensity profiles of input and output beams when the Δl is 2, 4, 6, 10, 14, and 18, respectively. The high-precision transfer of temporal characteristics is proved by the synchronous rotation period and direction of input and output beams with approximately 98% conversion accuracy at different Δf and Δl. The transfer of spatio-temporal OFW beams at different wavelengths holds the potential to drive significant advancements across optical microscopy and imaging, optical trapping and manipulation, as well as medical and biological applications.

REFERENCES

1. J. Wang, J. Yang, I. M. Fazal, *et al.*, "Terabit free-space data transmission employing orbital angular momentum multiplexing," Nat. Photonics **6**, 488–496 (2012).
2. M. P. Lavery, F. C. Speirits, S. M. Barnett, *et al.*, "Detection of a spinning object using light's orbital angular momentum," Science **341**, 537–540 (2013).
3. P. Xu, Y. Ma, J. Ren, *et al.*, "Satellite testing of a gravitationally induced quantum decoherence model," Science **366**, 132–135 (2019).
4. J. Yuan, H. Zhang, C. Wu, *et al.*, "Creation and control of vortex-beam arrays in atomic vapor," Laser Photon. Rev. **17**, 2200667 (2023).
5. Y. Zhang, M. Agnew, T. Roger, *et al.*, "Simultaneous entanglement swapping of multiple orbital angular momentum states of light," Nat. Commun. **8**, 632 (2017).
6. J. Yuan, W. Yang, M. Jing, *et al.*, "Quantum sensing of microwave electric fields based on Rydberg atoms," Rep. Prog. Phys. **86**, 106001 (2023).
7. Y. Shen, X. Wang, Z. Xie, *et al.*, "Optical vortices 30 years on: OAM manipulation from topological charge to multiple singularities," Light Sci. Appl. **8**, 90 (2019).
8. A. Chong, C. Wan, J. Chen, *et al.*, "Generation of spatiotemporal optical vortices with controllable transverse orbital angular momentum," Nat. Photonics **14**, 350–354 (2020).
9. Z. Li, R. Zhang, X. Yin, *et al.*, "Experimental quantum repeater without quantum memory," Nat. Photonics **13**, 644–648 (2019).
10. S. Franke-Arnold, J. Leach, M. J. Padgett, *et al.*, "Optical ferris wheel for ultracold atoms," Opt. Express **15**, 8619–8625 (2007).
11. T. Ando, N. Matsumoto, Y. Ohtake, *et al.*, "Structure of optical singularities in coaxial superpositions of Laguerre-Gaussian modes," J. Opt. Soc. Am. A **27**, 2602–2612 (2010).
12. M. Sakamoto, K. Oka, R. Morita, *et al.*, "Stable and flexible ring-shaped optical-lattice generation by use of axially symmetric polarization elements," Opt. Lett. **38**, 3661–3664 (2013).
13. L. Nie, L. Kong, T. Gao, *et al.*, "Characterizing the temporal rotation and radial twist of the interference pattern of vortex beams," Opt. Commun. **518**, 128339 (2022).
14. A. Asahara, S. Shoji, and K. Minoshima, "Optical combs and optical vortices combined for spatiotemporal manipulation of light and matter," arXiv, arXiv:2005.04705 (2020).
15. C. He, Y. Shen, and A. Forbes, "Towards higher-dimensional structured light," Light Sci. Appl. **11**, 205 (2022).
16. Z. Zhang, R. Wang, Y. Zhang, *et al.*, "Observation of edge solitons in photonic graphene," Nat. Commun. **11**, 1902 (2020).
17. A. Fleischer, O. Kfir, T. Diskin, *et al.*, "Spin angular momentum and tunable polarization in high-harmonic generation," Nat. Photonics **8**, 543–549 (2014).
18. M. T. Rakher, L. Ma, O. Slattery, *et al.*, "Quantum transduction of telecommunications-band single photons from a quantum dot by frequency upconversion," Nat. Photonics **4**, 786–791 (2010).
19. Z. Zhang, S. Liang, F. Li, *et al.*, "Spin-orbit coupling in photonic graphene," Optica **7**, 455–462 (2020).
20. N. Maring, D. Lago-Rivera, A. Lenhard, *et al.*, "Quantum frequency conversion of memory-compatible single photons from 606 nm to the telecom C-band," Optica **5**, 507–513 (2018).
21. T. Chaneliere, D. N. Matsukevich, S. D. Jenkins, *et al.*, "Quantum telecommunication based on atomic cascade transitions," Phys. Rev. Lett. **96**, 093604 (2006).
22. H. Cai, J. Liu, J. Wu, *et al.*, "Experimental observation of momentum-space chiral edge currents in room-temperature atoms," Phys. Rev. Lett. **122**, 023601 (2019).
23. S. Wang, J. Yuan, L. Wang, *et al.*, "Characterization of rubidium thin cell properties with sandwiched structure using a multipath interferometer with an optical frequency comb," Opt. Lett. **46**, 4284–4287 (2021).
24. J. Yuan, X. Cheng, X. Wang, *et al.*, "Single-scan polarization-resolved degenerate four-wave mixing spectroscopy using a vector optical field," Photon. Res. **10**, 230–236 (2022).
25. H. Li, J. Dou, X. Pang, *et al.*, "Heralding quantum entanglement between two room-temperature atomic ensembles," Optica **8**, 925–929 (2021).
26. Z. Zhang, Y. Feng, S. Ning, *et al.*, "Imaging lattice switching with Talbot effect in reconfigurable non-Hermitian photonic graphene," Photon. Res. **10**, 958–964 (2022).
27. G. Walker, A. S. Arnold, and S. Franke-Arnold, "Trans-spectral orbital angular momentum transfer via four-wave mixing in Rb vapor," Phys. Rev. Lett. **108**, 243601 (2012).
28. R. F. Offer, A. Daffurn, E. Riis, *et al.*, "Gouy phase-matched angular and radial mode conversion in four-wave mixing," Phys. Rev. A **103**, L021502 (2021).
29. R. F. Offer, A. Daffurn, E. Riis, *et al.*, "Spiral bandwidth of four-wave mixing in Rb vapour," Commun. Phys. **1**, 84 (2018).
30. D. Ding, Z. Zhou, B. Shi, *et al.*, "Linear up-conversion of orbital angular momentum," Opt. Lett. **37**, 3270–3273 (2012).
31. J. Yuan, X. Wang, G. Chen, *et al.*, "High-fidelity frequency converter in high-dimensional spaces," Laser Photon. Rev., 2400368 (2024).
32. Q. Zhao, M. Dong, Y. Bai, *et al.*, "Measuring high orbital angular momentum of vortex beams with an improved multipoint interferometer," Photon. Res. **8**, 745–749 (2020).
33. J. Guo, S. Zheng, K. Zhou, *et al.*, "Measurement of real phase distribution of a vortex beam propagating in free space based on an improved heterodyne interferometer," Appl. Phys. Lett. **119**, 023504 (2021).
34. A. Chopinaud, M. Jacquey, B. Viaris de Lesegno, *et al.*, "High helicity vortex conversion in a rubidium vapor," Phys. Rev. A **97**, 063806 (2018).
35. J. E. Curtis and D. G. Grier, "Structure of optical vortices," Phys. Rev. Lett. **90**, 133901 (2003).